crystals

MDPI

Article

Properties of SiC and Si_3N_4 Thin Films Containing Self-Assembled Gold Nanoparticles

Senad Isaković [1], Maja Đekić [1], Marija Tkalčević [2], Denis Boršćak [2], Ivana Periša [2], Sigrid Bernstorff [3] and Maja Mičetić [2,*]

[1] Faculty of Science, University of Sarajevo, Zmaja od Bosne 33, 71 000 Sarajevo, Bosnia and Herzegovina
[2] Ruđer Bošković Institute, Bijenička cesta 54, 10000 Zagreb, Croatia
[3] Elettra-Sincrotrone Trieste S.C.p.A., Strada Statale 14 km 163.5 in AREA Science Park, 34149 Trieste, Italy
* Correspondence: maja.micetic@irb.hr

Abstract: The properties of semiconductor materials can be strongly affected by the addition of metallic nanoparticles. Here we investigate the properties of SiC+Au and Si_3N_4+Au thin films prepared by magnetron sputtering deposition followed by thermal annealing. The influence of gold addition on the optical and electrical properties is explored. We show the formation of self-assembled Au nanoparticles in SiC and Si_3N_4, with the size and arrangement properties determined by the deposition and annealing conditions. Both SiC- and Si_3N_4-based films show an increase in the overall absorption with increasing Au content, and its decrease with increasing annealing temperature. All films show the presence of surface plasmon resonance, whose peaks shift toward larger wavelengths with increasing Au nanoparticle size. The resistivity significantly drops with the Au content increase for both types of matrices, although the resistivity of Si_3N_4-based films is much higher. The incorporated quantity of Au in the host matrix was chosen in such a way to demonstrate that a huge range of optical and electrical characteristics is achievable. The materials are very interesting for application in opto-electronic devices.

Keywords: SiC; Si_3N_4; Au nanoparticles; GISAXS; electrical resistivity; surface plasmon resonance

Citation: Isaković, S.; Đekić, M.; Tkalčević, M.; Boršćak, D.; Periša, I.; Bernstorff, S.; Mičetić, M. Properties of SiC and Si_3N_4 Thin Films Containing Self-Assembled Gold Nanoparticles. *Crystals* **2022**, *12*, 1361. https://doi.org/10.3390/cryst12101361

Academic Editors: Narmina O. Balayeva and Zamin Mamiyev

Received: 31 August 2022
Accepted: 22 September 2022
Published: 26 September 2022

1. Introduction

Silicon carbide (SiC) and silicon nitride (Si_3N_4) are materials with remarkable properties, such as wide band gap, high thermal conductivity, extreme hardness, and chemical inertness [1–10]. SiC is a semiconductor distinguished by high breakdown voltage and high electron drift velocity [11,12]. On the other hand, Si_3N_4 is a dielectric with good insulating properties. Therefore, they have been used extensively in the electronic industry for microelectronic devices and microelectromechanical systems (MEMS). They improved the silicon gate technology, and proved to be good passivation materials for power diodes and highly reliable power device substrates [13–16]. In addition, their application can be found in sensor and solar cell technology [17,18].

The properties of hitherto known materials can be significantly improved by the adjustment of their structure [19,20]. The most interesting structural adjustments intended for future technologies are reflected in the "insertions" of metal atoms, or nanostructures, into the host matrix [21,22]. In this context, SiC and Si_3N_4 matrices show significant potential for improving their basic electrical, mechanical, and optical properties [23–27].

The preparation and conditioning of nanostructures followed by their insertion in matrices depends on the dimensionality of functional material [28,29]. Depending on the application, nanostructures can exist as zero-dimensional quantum dots (QDs) [30,31],

one-dimensional nanofibers/nanotubes/nanorods [32,33], two-dimensional layered semiconductors/insulators, and three-dimensional complex structures [19,34].

In recent years, noble metal nanoparticles (NP) like gold (Au) and silver (Ag), embedded in host matrices, have become very promising candidates for both fundamental research and a variety of applications due to their unique mechanical, electrical, optical, and chemical properties. One of the main features of metal NPs arises during their interaction with an electromagnetic field. The applied field causes charge separation of electrons and ionic cores, thus creating dipole oscillations in the direction of the field. The maximum of the amplitude appears at a frequency called surface plasmon resonance (SPR) [35–37]. The exceptional plasmonic and optical properties of Au NPs have been extensively studied for applications such as: biosensoring [38], laser phototherapy of cancer cells and tumors [39,40], optical bio-imaging [41], water purification [42], photocatalysis [43], solar cells [44], and many more. In addition, a recent investigation of MoO_3 thin films containing self-organized Au NPs, prepared by simultaneous magnetron sputtering deposition, showed that the structural and optical properties of these films can be tailored for various applications in nanotechnology [45].

In this paper, we investigated structural, optical, and electrical properties of Au+SiC and Au+ Si_3N_4 thin films produced by magnetron sputtering codeposition. We demonstrate formation of Au NPs in both matrices differing by their size and arrangement properties. The size and separation of the NPs can be controlled by the deposition parameters and annealing temperature in the range of roughly 2–5 nm and 3–9 nm, respectively. The optical and electrical properties of the NPs depend strongly on the matrix in which they are embedded. The size and separation of the NPs formed in the carbide matrix increase with the Au concentration, and they have a stable structure upon annealing up to 500 °C. On the other hand, the size of Au NPs in the nitride matrix slightly increases with the annealing treatment. All NPs show SPR, with the shape and position dependent on their size and the matrix. The surface plasmons of the Au NPs embedded in the nitride matrix are significantly narrower than those in the carbide one. The films based on carbide matrices are generally more conductive, but the conductivity depends on the structural properties of the Au NPs as well.

2. Materials and Methods

Thin SiC+Au and Si_3N_4+ Au films were prepared by magnetron codeposition in a multi-source sputtering system (CMS-18 from K.J. Lesker company, Glassport, PA, USA) on Si(100) and glass substrates. We used 3-inch Au (99.999%), SiC (99.999%), and Si_3N_4 (99.999%) targets produced by K.J Lesker. The co-deposition of Au (DC-sputtering was used) and each of the matrices (SiC and Si_3N_4-RF sputtering mode was used) was performed at 400 °C for a duration of 1 h. The elevated temperature enabled formation of Au nanoparticles from the gold atoms during the deposition. The same procedure is used for production of different nanoparticles in dielectric matrices [31,34,35,45–47]. The base pressure in the chamber was 10^{-7} Pa, and the working gas (Ar) pressure was 0.46 Pa in a continuous flow. The samples were deposited as thin films at 3 different sputtering powers of Au in SiC (Au+SiC) and in Si_3N_4 (Au+ Si_3N_4) matrices, on Si (100) and glass substrates. The sputtering power for both matrices was 125 W. After the deposition, the films were annealed in a vacuum (pressure 10^{-5} mbar) at three different temperatures, so for each matrix material we have produced nine films differing by the amount of deposited gold and the annealing temperature. The samples were exposed to the atmosphere after the deposition and after the annealing. The deposition and annealing conditions, together with the sample names, film thicknesses, and Au-to-SiC/ Si_3N_4 volume ratios are summarized in Table 1.

The names of the samples are constructed as follows: The first letter of the film name represents the used matrix (C for SiC and N for Si_3N_4), followed by the number showing

the Au amount in the films (1, 2 and 3). The second part of the film name indicates the annealing temperature (T) of the film. Thus, the non-annealed film is marked with T1, while the film with the highest annealing temperature (500 °C) is marked with T3. For example, the SiC matrix with the smallest amount of Au annealed at 300 °C is named C1T2. The deposition conditions, together with the sample names, and Au-to-SiC/Si_3N_4 volume ratios are summarized in Table 1. The volume ratios are calculated from the structural parameters.

The structural analysis of the films (the nanoparticle formation, their size, and arrangement properties) was performed by Grazing-incidence small-angle X-ray scattering (GISAXS). Grazing incidence wide angle X-ray scattering (GIWAXS) was applied for the determination of the material's crystalline structure. Both measurement types were performed simultaneously at the Austrian SAXS-beamline of Elettra-Sincrotrone in Trieste, using 8 keV photons, a 2D 100k Pilatus (for GIWAXS) and a 2D Pilatus3 1M (for GISAXS) detector system (Dectris Ltd., Switzerland). The GISAXS and GIWAXS maps were measured using grazing incidence angles slightly above the critical angle.

Optical measurements were carried out using Ocean Optics equipment, including a deuterium-halogen light source (DH-2000-BAL), a UV/VIS detector and spectrometer (HR4000), and SpectraSuite software.

The transport properties of the films were investigated by the measurement of the surface resistance using the van der Pauw four contact method [48] at room temperature. Indium contacts were placed on the sample edges. All current-voltage (I-V) measurements were performed with a Keithley 2401 Sourcemeter SMU, while the LabView program was used for control and data collection.

Table 1. Deposition parameters of the films. P_{Au} indicates the sputtering power of Au, T_a is the annealing temperature, and Au to SiC/Si_3N_4 shows the targeted volume ratio of the Au to the matrix.

Sample/Par	P_{Au} (W)	T_a (°C)	Au to SiC Volume Ratio	Sample/Par	P_{Au} (W)	T_a (°C)	Au to Si_3N_4 Volume Ratio
C1T1	1	---	0.05	N1T1	1	---	0.08
C1T2	1	300	0.05	N1T2	1	300	0.08
C1T3	1	500	0.05	N1T3	1	500	0.08
C2T1	3	---	0.09	N2T1	3	---	0.11
C2T2	3	300	0.1	N2T2	3	300	0.11
C2T3	3	500	0.1	N2T3	3	500	0.12
C3T1	5	---	0.16	N3T1	5	---	0.2
C3T2	5	300	0.15	N3T2	5	300	0.2
C3T3	5	500	0.17	N3T3	5	500	0.2

3. Results and Discussion

3.1. Structural Properties of the Films

3.1.1. Nanoparticle Formation and Their Size-Arrangement Properties

The NP shape and size properties are analyzed using GISAXS technique. This technique provides data with excellent statistics (up to 10^{12} NPs in the illuminated volume), and it is proven in many similar systems to give accurate data in excellent agreement with microscopy measurements of the same film [49–54]. The GISAXS maps of the films are shown in Figure 1. Figure 1a shows the GISAXS maps of SiC+Au films, while Figure 1b shows GISAXS maps of Si_3N_4+Au thin films. All maps have a characteristic semicircular (ring-like) signal, which shows the presence of Au NPs that have a correlated mutual first neighbor spacing (inter-nanoparticle distance). In addition, all presented maps have features in the center that originate from the coherent scattering, surface roughness, and the entire film thickness contributions. However, these features are not interesting for the

analysis of the NP structural and arrangement properties. Therefore, our attention is fully devoted to the ring-like signal which decreases with increasing Au content in the films for both types of matrices (C1–C3 and N1–N3), showing an increase in the distance between the NPs and in the NP size.

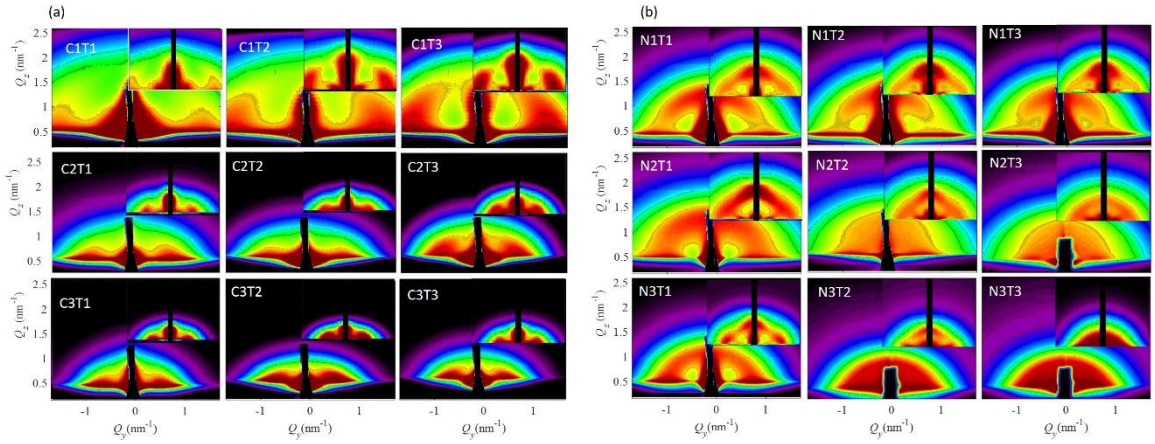

Figure 1. GISAXS maps of the investigated films. (**a**) Au NPs in SiC matrix, (**b**) Au NPs in Si_3N_4 matrix. The insets show the simulated GISAXS maps calculated using the parameters of the fit, given in Table 2.

To obtain the details of the structural properties, we performed a numerical analysis of the GISAXS maps using the model described in Reference [49]. More precisely, we assumed that the NPs order in a body-centered tetragonal lattice, panned by three basis vectors of which $\boldsymbol{a_1}$ and $\boldsymbol{a_2}$ are parallel to the substrate surface, while $\boldsymbol{a_3}$ describes the ordering of the NPs in the direction perpendicular to the film surface. A short-range ordering is assumed along all basis vectors. The irregularities in the NP lattice ordering, i.e., the deviations from the ideal positions defined by the basis vectors $\boldsymbol{a_1}$–$\boldsymbol{a_3}$, are described by four deviation parameters: ${\sigma_{1,2}}^{x,y}$, ${\sigma_3}^{x,y}$, and ${\sigma_{1,2}}^{z}$ describe the degree of deviation of the NP positions from the ideal ones in the direction parallel to the film substrate, while ${\sigma_3}^{z}$ describes the deviation in the direction perpendicular to the film substrate. The radii of the NPs are denoted by R_L and R_V for the directions parallel and perpendicular to the film substrate, respectively. The standard deviation of the size distribution is denoted by σ_R. For more details about the model used, and the relationship of the model and the parameters listed above, please see Reference [49]. The results of the numerical analysis are given in Table 2, while the simulated GISAXS maps, obtained using these parameters are given in insets of Figure 1.

Table 2. Parameters of the Au QD lattices found by GISAXS analysis and their errors. a and c are the lateral and vertical separation of Au NPs, respectively. ${\sigma_{1-3}}^{x,y,z}$ are the deviation parameters, σ_R is standard deviation of the size distribution, and R_L and R_V are the Au NP lateral and vertical radii, respectively. All values are given in nm.

Sample/Par.	$\boldsymbol{a}$	$\boldsymbol{c}$	$\boldsymbol{{\sigma_{1,2}}^{x,y}}$	$\boldsymbol{{\sigma_{1,2}}^{z}}$	$\boldsymbol{{\sigma_3}^{x,y}}$	$\boldsymbol{{\sigma_3}^{z}}$	$\boldsymbol{R_L}$	$\boldsymbol{R_V}$	$\boldsymbol{\sigma_R}$
C1T1	3.9 ± 0.3	3.9 ± 0.3	1.2 ± 0.2	1.0 ± 0.2	1.5 ± 0.2	0.9 ± 0.1	0.9 ± 0.2	1.0 ± 0.2	0.23 ± 0.08
C1T2	4.2 ± 0.3	4.2 ± 0.3	1.3 ± 0.2	1.1 ± 0.2	1.4 ± 0.2	0.9 ± 0.1	0.8 ± 0.2	1.1 ± 0.2	0.24 ± 0.07
C1T3	4.5 ± 0.3	4.5 ± 0.3	1.4 ± 0.2	1.1 ± 0.2	1.5 ± 0.2	1.0 ± 0.1	0.8 ± 0.2	1.0 ± 0.2	0.23 ± 0.08
C2T1	6.8 ± 0.2	4.8 ± 0.5	2.6 ± 0.2	2.2 ± 0.2	2.3 ± 0.2	1.7 ± 0.1	1.4 ± 0.2	2.1 ± 0.3	0.49 ± 0.08
C2T2	6.6 ± 0.2	4.5 ± 0.5	2.7 ± 0.2	1.9 ± 0.3	2.2 ± 0.3	1.9 ± 0.2	1.5 ± 0.2	2.3 ± 0.3	0.48 ± 0.09
C2T3	6.6 ± 0.2	4.5 ± 0.5	2.7 ± 0.3	2.2 ± 0.2	2.0 ± 0.3	1.7 ± 0.1	1.6 ± 0.3	2.0 ± 0.4	0.48 ± 0.08
C3T1	7.8 ± 0.2	6.9 ± 0.6	3.0 ± 0.3	1.7 ± 0.3	2.1 ± 0.3	2.2 ± 0.3	2.1 ± 0.3	2.7 ± 0.3	0.56 ± 0.08
C3T2	8.5 ± 0.2	6.5 ± 0.6	3.1 ± 0.3	1.9 ± 0.3	2.1 ± 0.3	2.3 ± 0.3	2.1 ± 0.3	2.9 ± 0.3	0.56 ± 0.08
C3T3	8.7 ± 0.2	6.2 ± 0.6	3.4 ± 0.3	2.3 ± 0.3	2.1 ± 0.3	2.2 ± 0.3	2.1 ± 0.3	2.3 ± 0.4	0.57 ± 0.09

N1T1	4.8 ± 0.2	4.4 ± 0.2	1.4 ± 0.2	1.9 ± 0.2	2.1 ± 0.2	1.3 ± 0.2	1.2 ± 0.2	1.4 ± 0.2	0.18 ± 0.04
N1T2	4.8 ± 0.2	4.4 ± 0.2	1.5 ± 0.2	2.2 ± 0.2	1.9 ± 0.2	1.3 ± 0.2	1.2 ± 0.2	1.4 ± 0.2	0.18 ± 0.04
N1T3	5.2 ± 0.2	4.4 ± 0.2	1.4 ± 0.2	2.3 ± 0.2	1.9 ± 0.2	1.3 ± 0.2	1.2 ± 0.2	1.5 ± 0.2	0.18 ± 0.04
N2T1	4.9 ± 0.2	4.5 ± 0.2	1.6 ± 0.2	1.8 ± 0.2	1.9 ± 0.2	1.3 ± 0.1	1.3 ± 0.2	1.4 ± 0.2	0.19 ± 0.05
N2T2	4.9 ± 0.5	4.5 ± 0.4	1.6 ± 0.4	2.5 ± 0.4	1.8 ± 0.3	1.4 ± 0.2	1.3 ± 0.2	1.5 ± 0.2	0.19 ± 0.04
N2T3	4.9 ± 0.5	5.3 ± 0.4	1.6 ± 0.4	3.3 ± 0.4	1.8 ± 0.3	1.8 ± 0.3	1.4 ± 0.2	1.5 ± 0.2	0.19 ± 0.04
N3T1	6.3 ± 0.2	4.6 ± 0.2	1.4 ± 0.1	2.0 ± 0.2	2.0 ± 0.2	1.3 ± 0.2	1.7 ± 0.2	2.1 ± 0.2	0.31 ± 0.05
N3T2	6.3 ± 0.5	4.6 ± 0.5	1.8 ± 0.4	3.4 ± 0.4	1.4 ± 0.4	1.8 ± 0.4	1.9 ± 0.2	2.2 ± 0.2	0.33 ± 0.06
N3T3	6.4 ± 0.5	4.9 ± 0.5	1.2 ± 0.4	1.2 ± 0.2	1.4 ± 0.4	1.8 ± 0.4	2.0 ± 0.2	2.2 ± 0.2	0.34 ± 0.06

The structural properties of the NPs in the SiC+Au and Si_3N_4+Au thin films, given in Table 2, are summarized in Figure 2. It shows the dependence of the structural parameters, i.e., the inter-NP separation a, the vertical separation c, the lateral NP radius R_L, and the vertical NP radisus R_V on annealing temperature for various Au sputtering powers. From Figure 2a–c, it follows that for the carbide matrix-based films all structural parameters increase with increasing Au sputtering power, while the annealing treatment has no significant effect. Similar results are obtained for the films based on the nitride matrix. The 3D lattice parameters tend to slightly increase with an increase in the Au sputtering power (Figure 2d–f), but the annealing has a more pronounced effect due to the nature of the nitride matrix, as will be discussed later. The effective radius of the Au NP increases slightly with both increasing Au sputtering power and annealing temperature.

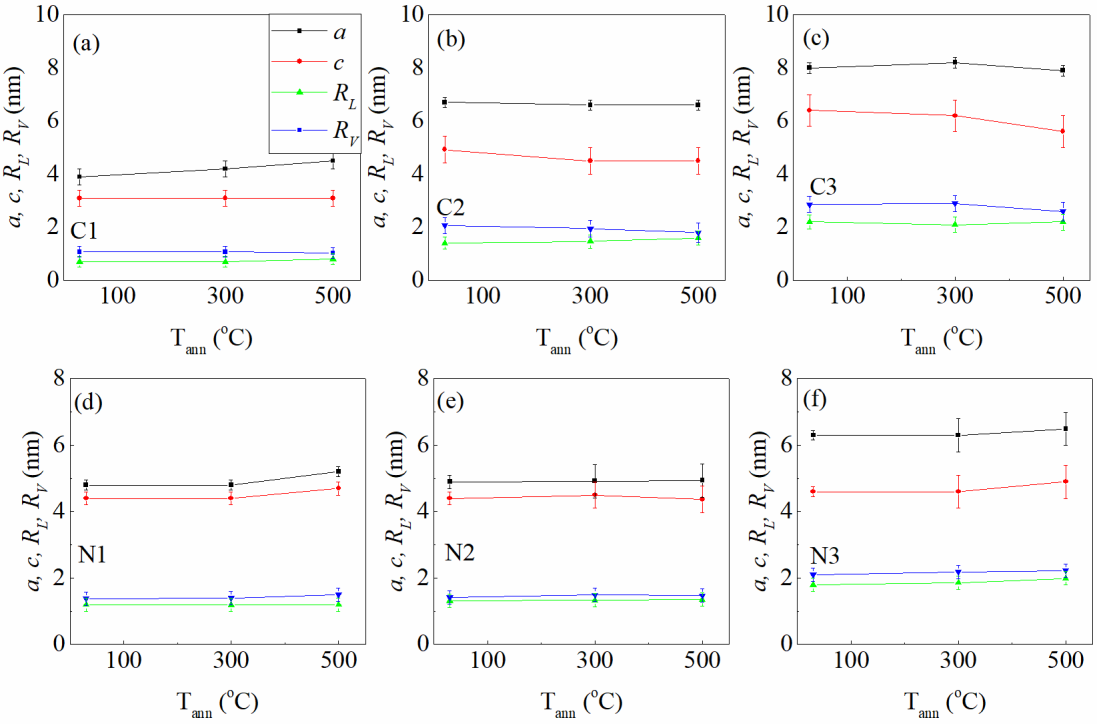

Figure 2. Dependence of the Au NP separations (*a*-lateral and *c*-vertical), and their effective radii (R_L and R_V) on the annealing temperature (T_{ann}) for (**a–c**) SiC matrix and (**d–f**) Si_3N_4 matrix.

3.1.2. Nanoparticle Internal Structure–Crystalline Properties

The GIWAXS analysis revealed the crystalline structure of the films. The measured curves are shown in Figure 3. Au NPs in SiC (Figure 3a–c) and Si_3N_4 matrices (Figure 3d–f) are represented by the peaks (111), (200), and (220) at 38.1, 44.3, and 64.5 degrees, respectively. The presence of the peaks clearly shows formation of crystalline gold NPs. The peaks are broad, especially for the films C1T1–C1T3, indicating a very small size of the formed Au NPs. For the same Au concentration, the width of the peaks does not change significantly with the annealing temperature. Therefore, the Au NPs are crystalline already after the deposition. However, a higher Au content induces narrower peaks, which is in agreement with the NP size increase found also by GISAXS analysis. The analysis of the width of the crystalline peaks using the Debye–Scherrer formula gives the rough estimation of the gold NP crystalline grain radii (R_c): R_c(C1) = 0.8 ± 0.2 nm, R_c (C2) = 1.2 ± 0.2 nm, R_c (C3) = 1.6 ± 0.4 nm, and R_c(N1) = 1.2 ± 0.2 nm, R_c (N2) = 1.4 ± 0.2 nm, R_c (N3) = 1.5 ± 0.4 nm. The average values for all three annealing temperatures of the same sample type are taken (for example, C1 is average for C1T1–C1T3), because this method provides a rough estimation only. However, the results are in good agreement with the GISAXS results, confirming formation of gold NPs.

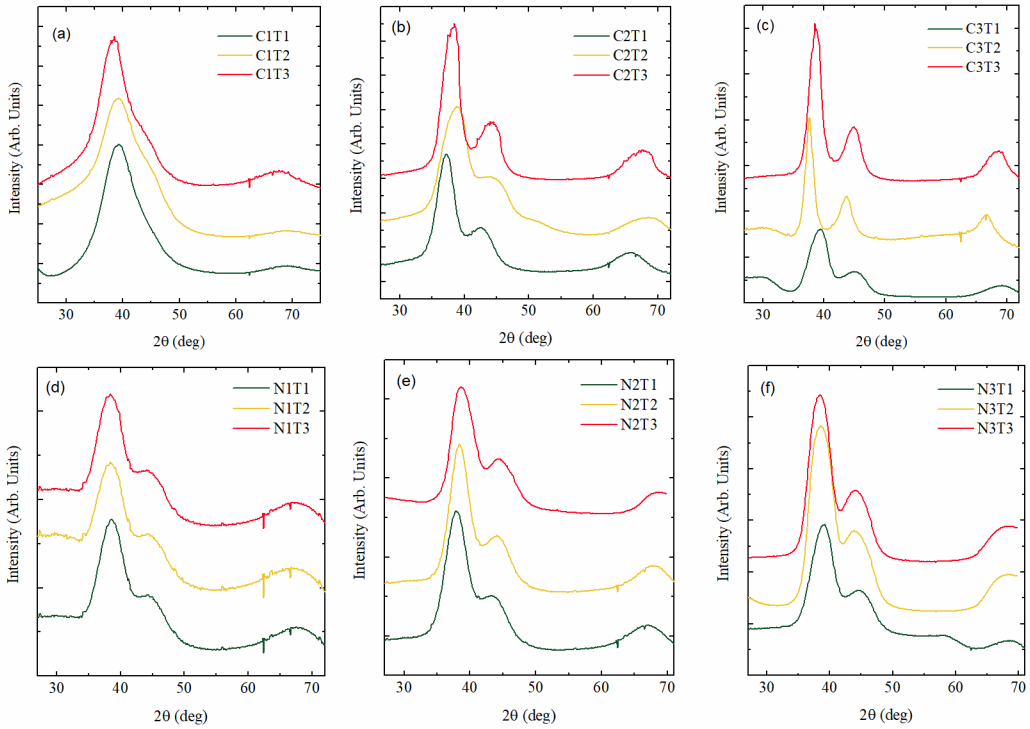

Figure 3. GIWAXS (grazing incidence wide angle X ray scattering) measurements of the Au NPs formed in (**a**–**c**) SiC and (**d**–**f**) Si_3N_4 matrices.

3.2. Optical Properties of the Films

The optical properties of the films (absorbance vs. wavelength) are shown in Figure 4. The absorption curves of the films are shown in Figure 4a–c for SiC-based films and in Figure 4d–f for Si_3N_4-based films. The value of the absorption increases with an increasing amount of Au for both types of matrices. Furthermore, the overall absorption slightly decreases with increasing annealing temperature at constant Au sputtering power (P_{Au}) for all samples. This trend can be explained by the variation in the absorption index of the

host matrix. For example, the absorption index of pure SiC thin film decreases with increasing annealing temperature, which is attributed to a relaxation of the network of the amorphous material [55].

All investigated films show the presence of Au surface plasmon resonances (SPR). To see better the properties of the SPR peaks, we have subtracted the matrix contribution to the absorptance. The obtained SPR contributions are shown in the insets of Figure 4. From the shown insets it is clear that the peak position, their width, and maximal intensity change significantly with the deposition conditions. These main properties of the peaks are analyzed and summarized in Table 3. The most obvious property is that the SPR peaks are much more pronounced for the nitride matrix, so their maximal intensity is about 10 times higher than for the peaks measured for the carbide matrix. The second clearly visible property is that the full width of the peaks at half maximum (FWHM) is smallest for the films with smaller gold NPs, and the widths are smaller for the nitride matrix than for the carbide. The largest difference in the SPR peak position is visible for the largest Au NPs. Thus, the SPR of the carbide matrix has a maximum of around 620 nm for the film with the largest Au NPs (Figure 4c), whereas the plasmon of the nitride matrix with the largest Au NPs (Figure 4f) has its maximum close to 570 nm. It is well known that the position of the SPR peak depends on the Au NP size and shape, and on the matrix properties, too [36]. It is clear from Figure 4 that for both the SiC and Si_3N_4 matrices, the plasmon peak shifts toward higher wavelengths (redshift) with increasing Au content (and Au NPs size). This shift is more pronounced in SiC-based thin films because the NP's size changes to a larger extent (see parameters R_L and R_V, Table 2). The observed shift of the SPR peak could be explained by the Mie theory, but it is shown that this theory is valid only for NPs of a diameter greater than 20 nm [56]. Our NPs are much smaller (smaller than 5 nm in diameter), and they approach the quantum size regime where both increased surface interactions and the quantum confinement affect the motion of electrons, which results in a Au optical constant modification. Therefore, in order to properly describe these modifications, which are the main reason for the observed redshift of the SPR peak, quantum mechanical effects, i.e., the discretization of the energy levels in the conduction band, must be taken into account [57]. On the basis of the above discussion, it could be concluded that, at constant sputtering power, the peaks will shift to higher wavelengths with an increase in the NP's size due to the annealing. However, not only is the NP affected by the annealing, it is also reported that the index of refraction decreases with increasing annealing temperature for both SiC and Si_3N_4 thin films [57]. Therefore, the reason for a slight shift of the SPR peak at constant Au sputtering power is competition of the blueshift, due to change in the optical properties of the host medium caused by annealing treatment and redshift due to the change in the NP's size [58].

As far as the peak width is concerned, the surface plasmons of the nitride matrix are significantly narrower that in the carbide one. Moreover, the width of the plasmon peaks in the SiC matrix are increasing with increasing Au NP's size. The narrowing of the peak is the consequence of the narrowing of the Au NPs' size distribution; the distribution is narrower for the nitride-based materials (see the parameter σ_R, Table 2).

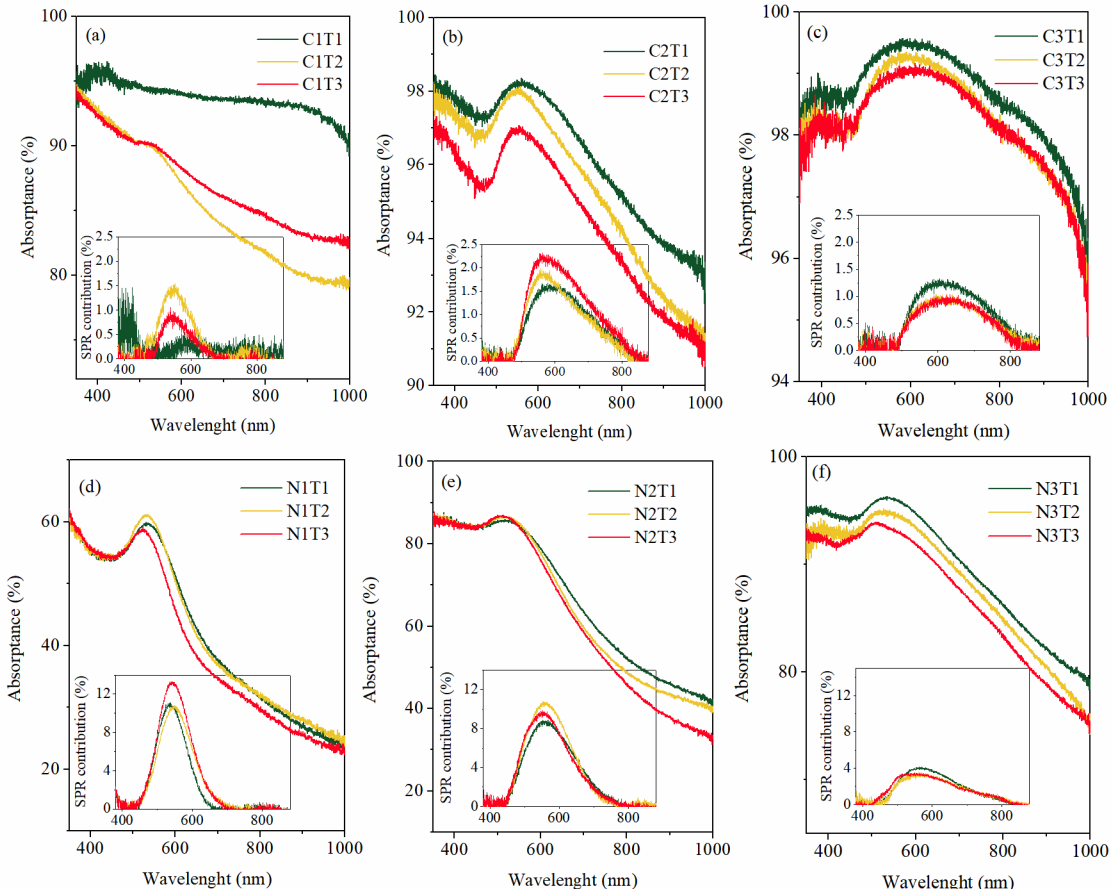

Figure 4. Optical properties of the films. Absorptance vs. wavelength for Au NPs in (**a**–**c**) SiC and (**d**–**f**) Si_3N_4 matrices. The insets show the SPR contribution in the absorptance. The x-scale in insets also represents the wavelength in nm.

Table 3. Parameters of the SPR contribution to the absorptance spectra. The peak position, its full width at half maximum (FWHM) and its maximal intensity (Peak max.) are shown. The unit of the maximum of the peak is percentage of the absorptance.

Par/Sample	**C1T1**	**C1T2**	**C1T3**	**C2T1**	**C2T2**	**C2T3**	**C3T1**	**C3T2**	**C3T3**
Peak pos. (nm)	590 ± 4	544 ± 2	542 ± 2	586	567	562	620	620	620
FWHM (nm)	132	102	96	197	184	210	254	255	255
Peak max. (%)	0.5	1.0	1.5	1.5	1.9	2.2	1.3	1.0	1.0
Par/sample	**N1T1**	**N1T2**	**N1T3**	**N2T1**	**N2T2**	**N2T3**	**N3T1**	**N3T2**	**N3T3**
Peak pos. (nm)	537	550	541	560	555	558	570	570	549
FWHM (nm)	101	107	111	157	150	148	200	201	211
Peak max. (%)	10.8	10.7	13.0	8.8	9.8	10.6	4.0	3.3	3.3

3.3. Electrical Properties of the Films

The dependence of the measured sheet resistance of the films on the annealing temperature is given in Figure 5. Figure 5a,b show the sheet resistance of SiC-based and Si_3N_4-based thin films, respectively. Both materials show a significant dependence on the resistance of the Au concentration, as it strongly drops with an increasing Au amount. The sheet resistance of the SiC films slightly increases with increasing annealing temperature, up to 300 °C, while for 500 °C a drop occurs. This is evident in the films with the highest and the smallest amount of Au. On the other hand, in C2 samples, the resistivity increases with increasing annealing temperature for the whole temperature range. The values of the measured sheets' resistances are significantly smaller than those measured for pure SiC

films, approximately 100 to 300 times (according to pure SiC data in Ref. [12]) for the lowest and highest Au concentration (C1 and C3).

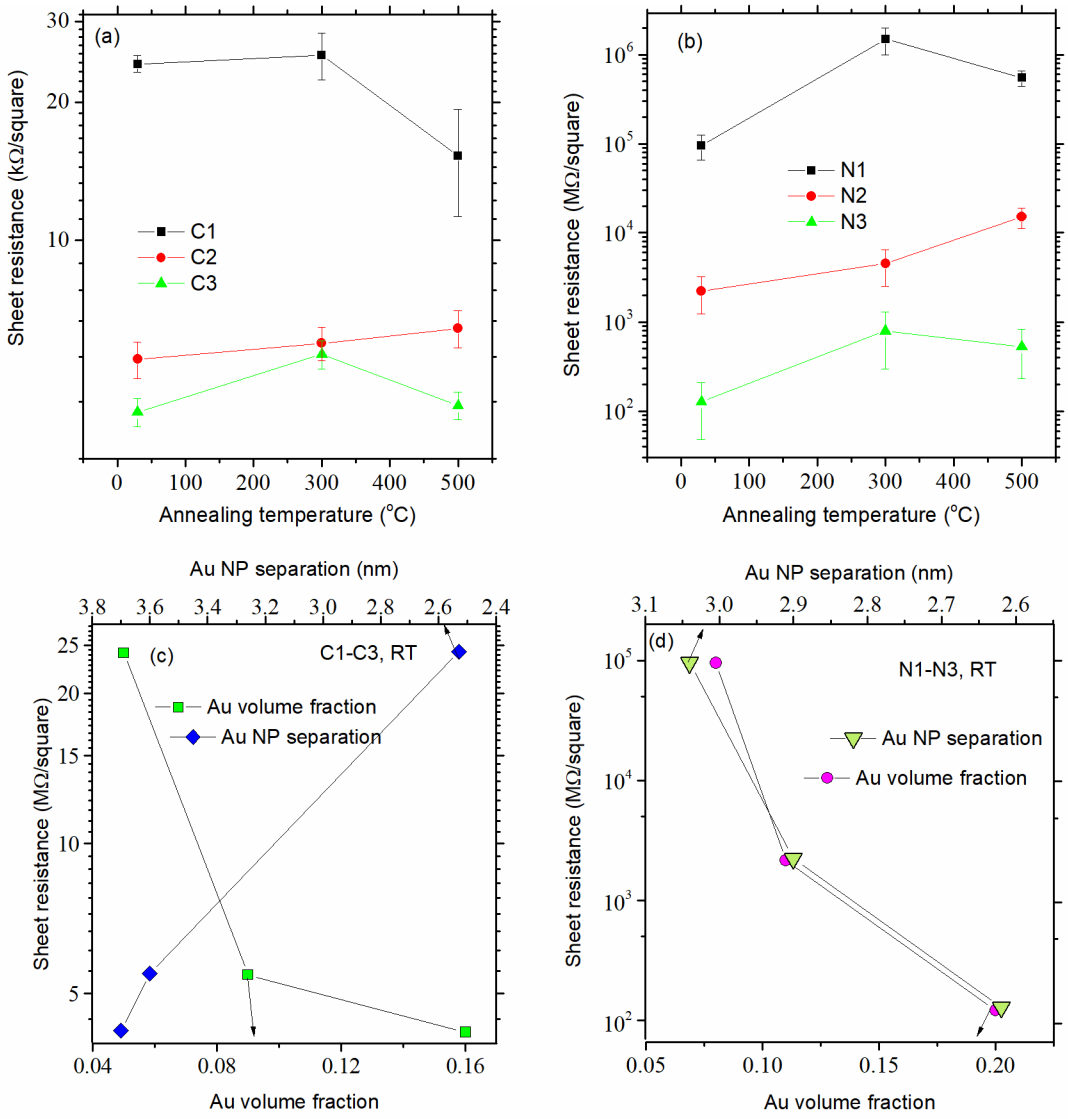

Figure 5. Sheet resistance as a function of annealing temperature of (**a**) SiC-based and (**b**) Si_3N_4-based films. Dependence of sheet resistance on Au volume fraction and averaged Au NP separation in (**c**) SiC-based and (**d**) Si_3N_4-based films.

In pure SiC thin film, the dominant role in transport mechanism at room temperature is hopping between localized states [59,60]. Transport mechanisms can be controlled by the deposition conditions. For example, the conductivity of amorphous SiC thin film depends significantly on the porosity of the material introduced by the deposition conditions [60]. Although, in recent investigations many different deposition parameters were examined, films with a resistivity of less than 200 kΩcm could not be obtained [61]. The smallest obtained resistivity is still about two orders of magnitude larger than the resistivity of Au-based films deposited in the SiC matrix that we have produced. Thus, we believe that the origin of the resistance decrease with increasing Au volume fraction (Figure 5c) might be due to the increase in electron density of localized states near the Fermi level caused by the insertion of Au nanoparticles. This assumption is supported by the dependence of resistance on the Au NP separation, also shown on Figure 5c. Nevertheless, increasing the Au volume fraction in the unite cell of the SiC matrix might lead to the tunneling between Au NPs, but the decrease in the resistance with increasing Au NP separation suggests that

the hopping between localized states is still the dominant transport mechanism. The separations between the NPs are quite large for the tunneling (3.6 nm and 3.7 nm for films C1 and C2), which also supports the given assumption. On the other side, the film with C1 has the largest Au NP surface to volume ratio, due to the formation of large number of small Au NPs.

Figure 5b shows the sheet resistance of the Si_3N_4-based films. Here, in regard to SiC-based films, the resistance is significantly higher because amorphous Si_3N_4 is dielectric in nature. It is evident that the Au content in the films significantly influences the resistivity. Thus, as the Au volume fraction (Figure 5d) in the films is increased, the resistivity drops dramatically. The resistivity of N2 samples is two orders of magnitude smaller than for N1 samples, while the drop in resistance is even higher for N3 samples (about three orders of magnitude). The Au NP separation for the nitride-based films is smaller than for the SiC case (3.05 nm to 2.6 nm for films N1 to N3), so the tunneling between the NPs is much more probable. The dependence of the resistivity on the Au NP separation agreed excellently with its dependence on the Au volume fraction in the case of the nitride matrix, as visible from Figure 5d. Therefore, in the case of dielectric Si_3N_4 matrix, which is much more resistant than SiC, tunneling is the main transport mechanism. However, the resistance might also be affected by the number of silicon dangling bonds [62]. The number of Si dangling bonds depends on the content of nitrogen and on the annealing temperature. It was shown that for annealing at 500 °C some of Si-N bonds broke and the resistance of the films began to drop [63]. Figure 5b shows that the samples with the smallest Au amount and the largest Au NP separation (N1) exhibit a similar behavior. On the other hand, when the content of Au is increased, like in the N2 and N3 samples, the dependence of the resistance on the number of Si dangling bonds and on the content of nitrogen can be neglected. Here, the dominant role in the transport mechanism is taken over by the tunneling between Au NPs.

4. Conclusions

We studied Au+SiC and Au+Si_3N_4 thin films prepared by magnetron sputtering co-deposition and annealed at temperatures low enough to avoid crystallization of the amorphous matrices and the evaporation of gold. The parameters of the Au nanoparticles and structural parameters of these films, together with their main optical and transport properties, were explored. A detailed structural analysis shows that Au forms sphere-like NPs in both the SiC and Si_3N_4 matrices. The Au NPs turned out to be well arranged in a 3D lattice. It was possible to show the relationship between the parameters of the Au NP lattice and the deposition condition. Moreover, adjusting the sputtering power and annealing temperature results in tunable dimensions and arrangement properties of the Au NPs. The UV-VIS absorption spectra of the SiC- and Si_3N_4-based films are very similar. All films show a decrease in the absorption with decreasing Au content and increasing annealing temperature. In addition, they show a size- and temperature-dependent surface plasmon resonance peak. This SPR peak redshifts with increasing Au NP size for both types of matrices. The temperature-dependence of the SPR peak position is not so clear because, besides the Au NP size, the matrix optical constant changes with annealing treatment as well. As far as the peak width is concerned, the surface plasmons of the nitride matrix are significantly narrower than in the carbide one. The investigated films show the same trend in the resistivity. The resistivity of both the SiC- and Si_3N_4-based films increases with increasing Au content. The resistivity of the films decreases significantly with the Au concentration. The drop is especially pronounced for the nitride-based films, where the change by several orders of magnitude are found. The main charge transport properties in the silicon-carbide based films are governed by the structure of SiC matrix, while tunneling between the Au NPs is the main transport mechanism in the nitride-based films.

All studied materials have a huge application potential, in everything from biomedicine to nanotechnologies.

Author Contributions: Conceptualization, S. I. and M.M.; methodology, S. I., S.B., and M.M.; software, M.M.; formal analysis, S.I., M. Đ., I.P., D.B. and M.M.; data curation, S.I., I.P., D.B., M.T. and S.B.; writing—original draft preparation, S.I. and M.M. ; writing—review and editing, all authors; visualization, S.I., M.Đ. and M.M.; project administration, M.M.; funding acquisition, M.M. All authors have read and agreed to the published version of the manuscript.

Funding: This research was funded by the Croatian Science Foundation (No. IP-2018-01-3633 and DOK-2018-09-5383) and the Center of Excellence for Advanced Materials and Sensing Devices (Grant KK.01.1.1.01.0001). The authors acknowledge the CERIC-ERIC Consortium for the access to the experimental SAXS facilities and financial support.

Data Availability Statement: The data available at Mičetić, Maja (2022), "Properties of SiC and Si3N4 Thin Films Containing Self-Assembled Gold Nanoparticles", Mendeley Data, V1, doi: 10.17632/n298gcwbrf.1

Acknowledgments: The authors thank J. Erceg for the assistance in the sample preparation and D. Mičetić for GISAXS measurements.

Conflicts of Interest: The authors declare no conflict of interest. The funders had no role in the design of the study; in the collection, analyses, or interpretation of data; in the writing of the manuscript, or in the decision to publish the results.

References

1. Kim, J.H.; Chung, K.W. Microstructure and properties of silicon nitride thin films deposited by reactive bias magnetron sputtering. *J. Appl. Phys.* **1998**, *83*, 5831–5839. https://doi.org/10.1063/1.367440.
2. Zhang, S.; Raniero, L.; Fortunato, E.; Pereira, L.; Martins, N.; Canhola, P.; Ferreira, I.; Nedev, N.; Águas, H.; Martins, R. Characterization of silicon carbide thin films prepared by VHF-PECVD technology. *J. Non-Cryst. Solids* **2004**, *338–340*, 530–533. https://doi.org/10.1016/j.jnoncrysol.2004.03.035.
3. Tehrani, F.S.; Fakhredin, M.; Tafreshi, M.J. The optical properties of silicon carbide thin films prepared by HWCVD from pure silane and methane under various total gas partial pressure. *Mater. Res. Express* **2019**, *6*, 086469. https://doi.org/10.1088/2053-1591/ab2843.
4. Morkoç, H.; Strite, S.; Gao, G.B.; Lin, M.E.; Sverdlov, B.; Burns, M. Large-band-gap SiC, III-V nitride, and II-VI ZnSe-based semiconductor device technologies. *J. Appl. Phys.* **1994**, *76*, 1363–1398. https://doi.org/10.1063/1.358463.
5. Lattemann, M.; Nold, E.; Ulrich, S.; Leiste, H.; Holleck, H. Investigation and characterisation of silicon nitride and silicon carbide thin films. *Surf. Coat. Technol.* **2003**, *174–175*, 365–369. https://doi.org/10.1016/S0257-8972(03)00695-9.
6. Choi, S.R.; Kim, D.; Choa, S.-H.; Lee, S.-H.; Kim, J.-K. Thermal Conductivity of AlN and SiC Thin Films. *Int. J. Thermophys.* **2006**, *27*, 896–905. https://doi.org/10.1007/s10765-006-0062-1.
7. Su, G.-P.; Zheng, X.-H.; Qiu, L.; Tang, D.-W.; Zhu, J. Measurement of Thermal Conductivity of Anisotropic SiC Crystal. *Int. J. Thermophys.* **2013**, *34*, 2334–2342. https://doi.org/10.1007/s10765-012-1163-7.
8. Liu, A.Y.; Cohen, M.L. Structural properties and electronic structure of low-compressibility materials: β-Si_3N_4 and hypothetical β-Si_3N_4. *Phys. Rev. B* **1990**, *41*, 10727–10734. https://doi.org/10.1103/PhysRevB.41.10727.
9. Vila, M.; Cáceres, D.; Prieto, C. Mechanical properties of sputtered silicon nitride thin films. *J. Appl. Phys.* **2003**, *94*, 7868. https://doi.org/10.1063/1.1626799.
10. Zhang, X.; Grigoropoulos, C.P. Thermal conductivity and diffusivity of free-standing silicon nitride thin films. *Rev. Sci. Instrum.* **1995**, *66*, 1115–1120. https://doi.org/10.1063/1.1145989.
11. Brassard, D.; el Khakani, M.A. Dielectric properties of amorphous hydrogenated silicon carbide thin films grown by plasma-enhanced chemical vapor deposition. *J. Appl. Phys.* **2003**, *93*, 4066–4071. https://doi.org/10.1063/1.1555676.
12. Zhou, J.; Zheng, X. Structure and electronic properties of SiC thin-films deposited by RF magnetron sputtering. *Trans. Nonferrous Met. Soc. China* **2007**, *17*, 373–377. https://doi.org/10.1016/S1003-6326(07)60101-0.
13. Ledermann, N.; Baborowski, J.; Muralt, P.; Xantopoulos, N.; Tellenbach, J.-M. Sputtered silicon carbide thin films as protective coating for MEMS applications. *Surf. Coat. Technol.* **2000**, *125*, 246–250. https://doi.org/10.1016/S0257-8972(99)00568-X.
14. Bhatt, V.; Chandra, S. Silicon Nitride Films Deposited by RF Sputtering for Microstructure Fabrication in MEMS. *J. Elec. Mater.* **2009**, *38*, 1979–1989. https://doi.org/10.1007/s11664-009-0846-8.
15. Isoird, K.; Lazar, M.; Ottaviani, L.; Locatelli, M.L.; Raynaud, C.; Planson, D.; Chante, J.P. Study of 6H–SiC high voltage bipolar diodes under reverse biases. *Appl. Surf. Sci.* **2001**, *184*, 477–482. https://doi.org/10.1016/S0169-4332(01)00537-2.
16. Dow, H.S.; Kim, W.S.; Lee, J.W. Thermal and electrical properties of silicon nitride substrates. *AIP Adv.* **2017**, *7*, 095022. https://doi.org/10.1063/1.4996314.

17. Solzbacher, F.; Imawan, C.; Steffes, H.; Obermeier, E.; Eickhoff, M. A highly stable SiC based microhotplate NO_2 gas-sensor. *Sens. Actuators B Chemical.* **2001**, *78*, 216–220. https://doi.org/10.1016/S0925-4005(01)00815-2.
18. Kaloyeros, A.E.; Jové, F.A.; Goff, J.; Arkles, B. Review—Silicon Nitride and Silicon Nitride-Rich Thin Film Technologies: Trends in Deposition Techniques and Related Applications. *ECS J. Solid State Sci. Technol.* **2017**, *6*, P691–P714. https://doi.org/10.1149/2.0011710jss.
19. Miranzo, P.; García, E.; Ramírez, C.; González-Julián, J.; Belmonte, M.; Osendi, M.I. Anisotropic thermal conductivity of silicon nitride ceramics containing carbon nanostructures. *J. Eur. Ceram. Soc.* **2012**, *32*, 1847–1854. https://doi.org/10.1016/j.jeurceramsoc.2012.01.026.
20. Taube, W.R.; Kumar, A.; Saravanan, R.; Agarwal, P.B.; Kothari, P.; Joshi, B.C.; Kumar, D. Efficiency enhancement of silicon solar cells with silicon nanocrystals embedded in PECVD silicon nitride matrix. *Sol. Energy Mater. Sol. Cells* **2012**, *101*, 32–35. https://doi.org/10.1016/j.solmat.2012.02.010.
21. Kim, S.-H.; Jang, K.; Kang, P.W.; Ahn, J.-P.; Seol, J.-B.; Kwak, C.-M.; Hatzoglou, C.; Vurpillot, F.; Choi, P.-P. Characterization of Pd and Pd@Au core-shell nanoparticles using atom probe tomography and field evaporation simulation. *J. Alloys Compd.* **2020**, *831*, 154721. https://doi.org/10.1016/j.jallcom.2020.154721.
22. Huo, N.; Kang, J.; Wei, Z.; Li, S.-S.; Li, J.; Wei, S.-H. Novel and Enhanced Optoelectronic Performances of Multilayer MoS_2-WS_2 Heterostructure Transistors. *Adv. Funct. Mater.* **2014**, *24*, 7025–7031. https://doi.org/10.1002/adfm.201401504.
23. Johannesson, D.; Nawaz, M.; Jacobs, K.; Norrga, S.; Nee, H.-P. Potential of ultra-high voltage silicon carbide semiconductor devices. In Proceedings of the 2016 IEEE 4th Workshop on Wide Bandgap Power Devices and Applications (WiPDA), IEEE, Fayetteville, AR, USA, 7–9 November 2016; pp. 253–258. https://doi.org/10.1109/WiPDA.2016.7799948.
24. Lagier, T.; Ladoux, P.; Dworakowski, P. Potential of silicon carbide MOSFETs in the DC/DC converters for future HVDC offshore wind farms. *High Volt.* **2017**, *2*, 233–243. https://doi.org/10.1049/hve.2017.0070.
25. Nazarkovsky, M.; Alekseev, S.; Huczko, A.; Zaitsev, V.; Dupont, J.; Kai, J.; Xing, Y.; Scofield, A.L.; Chacón, G.; Carreira, R.S. Structural and photocatalytic properties of silicon carbide powder and nanowires modified by gold nanoparticles. *Res. Chem. Intermed.* **2019**, *45*, 4081–4100. https://doi.org/10.1007/s11164-019-03892-3.
26. Klemm, H. Silicon Nitride for High-Temperature Applications: Silicon Nitride for High-Temperature Applications. *J. Am. Ceram. Soc.* **2010**, *93*, 1501–1522. https://doi.org/10.1111/j.1551-2916.2010.03839.x.
27. Kaloyeros, A.E.; Pan, Y.; Goff, J.; Arkles, B. Review—Silicon Nitride and Silicon Nitride-Rich Thin Film Technologies: State-of-the-Art Processing Technologies, Properties, and Applications. *ECS J. Solid State Sci. Technol.* **2020**, *9*, 063006. https://doi.org/10.1149/2162-8777/aba447.
28. Rajendran, R.; Shrestha, L.K.; Minami, K.; Subramanian, M.; Jayavel, R.; Ariga, K. Dimensionally integrated nanoarchitectonics for a novel composite from 0D, 1D, and 2D nanomaterials: RGO/CNT/CeO_2 ternary nanocomposites with electrochemical performance. *J. Mater. Chem. A* **2014**, *2*, 18480–18487. https://doi.org/10.1039/C4TA03996C.
29. Bernstorff, S.; Holý, V.; Endres, J.; Valeš, V.; Sobota, J.; Siketić, Z.; Bogdanović-Radović, I.; Buljan, M.; Dražić, G. Co nanocrystals in amorphous multilayers—A structure study. *J. Appl. Crystallogr.* **2013**, *46*, 1711–1721. https://doi.org/10.1107/S0021889813026836.
30. Zhu, S.; Song, Y.; Zhao, X.; Shao, J.; Zhang, J.; Yang, B. The photoluminescence mechanism in carbon dots (graphene quantum dots, carbon nanodots, and polymer dots): Current state and future perspective. *Nano Res.* **2015**, *8*, 355–381. https://doi.org/10.1007/s12274-014-0644-3.
31. Nekić, N.; Šarić, I.; Salamon, K.; Basioli, L.; Sancho-Parramon, J.; Grenzer, J.; Hübner, R.; Bernstorff, S.; Petravić, M.; Mičetić, M. Preparation of non-oxidized Ge quantum dot lattices in amorphous Al_2O_3, Si_3N_4 and SiC matrices. *Nanotechnology* **2019**, *30*, 335601. https://doi.org/10.1088/1361-6528/ab1d3c.
32. Melanko, J.B.; Pearce, M.E.; Salem, A.K. Nanotubes, Nanorods, Nanofibers, and Fullerenes for Nanoscale Drug Delivery. In *Nanotechnology in Drug Delivery*; de Villiers, M.M., Aramwit, P., Kwon, G.S., Eds.; Springer: New York, NY, USA, 2009; pp. 105–127. https://doi.org/10.1007/978-0-387-77668-2_4.
33. Balázsi, C.; Wéber, F.; Kövér, Z.; Shen, Z.; Kónya, Z.; Kasztovszky, Z.; Vértesy, Z.; Biró, L.P.; Kiricsi, I.; Arató, P. Application of carbon nanotubes to silicon nitride matrix reinforcements. *Curr. Appl. Phys.* **2006**, *6*, 124–130. https://doi.org/10.1016/j.cap.2005.07.024.
34. Basioli, L.; Tkalčević, M.; Bogdanović-Radović, I.; Dražić, G.; Nadazdy, P.; Siffalovic, P.; Salamon, K.; Mičetić, M. 3D Networks of Ge Quantum Wires in Amorphous Alumina Matrix. *Nanomaterials* **2020**, *10*, 1363. https://doi.org/10.3390/nano10071363.
35. Borges, J.; Buljan, M.; Sancho-Parramon, J.; Bogdanović-Radović, I.; Siketić, Z.; Scherer, T.; Kübel, C.; Bernstorff, S.; Cavaleiro, A.; Vaz, F.; et al. Evolution of the surface plasmon resonance of Au:TiO_2 nanocomposite thin films with annealing temperature. *J. Nanopart. Res.* **2014**, *16*, 2790. https://doi.org/10.1007/s11051-014-2790-7.
36. Amendola, V.; Pilot, R.; Frasconi, M.; Maragò, O.M.; Iatì, M.A. Surface plasmon resonance in gold nanoparticles: A review. *J. Phys. Condens. Matter* **2017**, *29*, 203002. https://doi.org/10.1088/1361-648X/aa60f3.
37. Yao, G.-Y.; Liu, Q.-L.; Zhao, Z.-Y. Studied Localized Surface Plasmon Resonance Effects of Au Nanoparticles on TiO_2 by FDTD Simulations. *Catalysts* **2018**, *8*, 236. https://doi.org/10.3390/catal8060236.
38. Haes, A.J.; van Duyne, R.P. A Nanoscale Optical Biosensor: Sensitivity and Selectivity of an Approach Based on the Localized Surface Plasmon Resonance Spectroscopy of Triangular Silver Nanoparticles. *J. Am. Chem. Soc.* **2002**, *124*, 10596–10604. https://doi.org/10.1021/ja020393x.

39. Huang, X.; El-Sayed, I.H.; Qian, W.; El-Sayed, M.A. Cancer Cell Imaging and Photothermal Therapy in the Near-Infrared Region by Using Gold Nanorods. *J. Am. Chem. Soc.* **2006**, *128*, 2115–2120. https://doi.org/10.1021/ja057254a.
40. Hirsch, L.R.; Stafford, R.J.; Sershen, S.R.; Halas, N.J.; Hazle, J.D.; West, J.L. Nanoshell-assisted tumor ablation using near infrared light under magnetic resonance guidance. *Proc Natl Acad Sci. USA* **2003**, *100*, 113549–54.
41. Dykman, L.A.; Khlebtsov, N.G. Gold Nanoparticles in Biology and Medicine: Recent Advances and Prospects. *Acta Nat.* **2011**, *3*, 34–55.
42. Qian, H.; Pretzer, L.A.; Velazquez, J.C.; Zhao, Z.; Wong, M.S. Gold nanoparticles for cleaning contaminated water: Gold nanoparticles for cleaning contaminated water. *J. Chem. Technol. Biotechnol.* **2013**, *88*, 735–741. https://doi.org/10.1002/jctb.4030.
43. Martins, P.; Kappert, S.; Le, H.N.; Sebastian, V.; Kühn, K.; Alves, M.; Pereira, L.; Cuniberti, G.; Melle-Franco, M.; Lanceros-Méndez, S. Enhanced Photocatalytic Activity of Au/TiO_2 Nanoparticles against Ciprofloxacin. *Catalysts* **2020**, *10*, 234. https://doi.org/10.3390/catal10020234.
44. Atwater, H.A.; Polman, A. Plasmonics for Improved Photovoltaic Devices. *Nature Mater* **2010**, *9, 205–213 https://doi.org/10.1038/nmat2629*
45. Car, T.; Jakovac, I.; Šarić, I.; Bernstorff, S.; Micetic, M. Structural, Optical and Electrical Properties of Al+MoO_3 and Au+MoO_3 Thin Films Prepared by Magnetron Codeposition. *Materials* **2021**, *14*, 766. https://doi.org/10.3390/ma14040766.
46. Okumu, J.; Dahmen, C.; Sprafke, A.N.; Luysberg, M.; von Plessen, G.; Wuttig, M. Photochromic silver nanoparticles fabricated by sputter deposition. *J. Appl. Phys.* **2005**, *97*, 094305. https://doi.org/10.1063/1.1888044.
47. Hatakeyama, Y.; Onishi, K.; Nishikawa, K. Effects of sputtering conditions on formation of gold nanoparticles in sputter deposition technique. *RSC Adv.* **2011**, *1*, 1815–1821. https://doi.org/10.1039/C1RA00688F.
48. Van der Pauw, L.J.A. A method of measuring the resistivity and Hall coefficient on lamellae of arbitrary shape. *Philips Tech. Rev.* **1958**, *26*, 220–224.
49. Buljan, M.; Radić, N.; Bernstorff, S.; Dražić, G.; Bogdanović-Radović, I.; Holý, V. Grazing-incidence small-angle X-ray scattering: Application to the study of quantum dot lattices. *Acta Crystallogr. Found Crystallogr.* **2012**, *68*, 124–138. https://doi.org/10.1107/S0108767311040104.
50. Basioli, L.; Salamon, K.; Tkalčević, M.; Mekterović, I.; Bernstorff, S.; Mičetić, M. Application of GISAXS in the Investigation of Three-Dimensional Lattices of Nanostructures. *Crystals* **2019**, *9*, 479. https://doi.org/10.3390/cryst9090479.
51. Buljan, M.; Radić, N.; Ivanda, M.; Bogdanović-Radović, I.; Karlušić, M.; Grenzer, J.; Prucnal, S.; Dražić, G.; Pletikapić, G.; Svetličić, V.; et al. Ge quantum dot lattices in Al_2O_3 multilayers. *J. Nanoparticle Res.* **2013**, *15*, 1485. https://doi.org/10.1007/s11051-013-1485-9.
52. Pinto, S.R.C.; Rolo, A.G.; Buljan, M.; Chahboun, A.; Bernstorff, S.; Barradas, N.P.; Alves, E.; Kashtiban, R.J.; Bangert, U.; Gomes, M.J.M. Low-temperature fabrication of layered self-organized Ge clusters by RF sputtering. *Nanoscale Res. Lett.* **2011**, *6*, 341. https://doi.org/10.1186/1556-276X-6-341.
53. Buljan, M.; Radić, N.; Sancho-Paramon, J.; Janicki, V.; Grenzer, J.; Bogdanović-Radović, I.; Siketić, Z.; Ivanda, M.; Utrobičić, A.; Hübner, R.; et al. Production of three-dimensional quantum dot lattice of Ge/Si core–shell quantum dots and Si/Ge layers in an alumina glass matrix. *Nanotechnology* **2015**, *26*, 065602. https://doi.org/10.1088/0957-4484/26/6/065602.
54. Nekić, N.; Parramon, J.S.; Bogdanović-Radović, I.; Grenzer, J.; Huebner, R.; Ivanda, M.; Buljan, M. Ge/Si core/shell quantum dots in alumina: Tuning the optical absorption by the core and shell size. *Nanophotonics* **2017**, *6*, 1055–1062. https://doi.org/10.1515/nanoph-2016-0133.
55. Musumeci, P.; Reitano, R.; Calcagno, L.; Roccaforte, F.; Makhtari, A.; Grimaldi, M.G. Relaxation and crystallization of amorphous silicon carbide probed by optical measurements. *Philos. Mag. B* **1997**, *76*, 323–333. https://doi.org/10.1080/01418639708241097.
56. Jain, P.K.; Lee, K.S.; El-Sayed, I.H.; El-Sayed, M.A. Calculated Absorption and Scattering Properties of Gold Nanoparticles of Different Size, Shape, and Composition: Applications in Biological Imaging and Biomedicine. *J. Phys. Chem. B* **2006**, *110*, 7238–7248. https://doi.org/10.1021/jp057170o.
57. Scholl, J.A.; Koh, A.L.; Dionne, J.A. Quantum plasmon resonances of individual metallic nanoparticles. *Nature* **2012**, *483*, 421–427. https://doi.org/10.1038/nature10904.
58. Singhal, R.; Kabiraj, D.; Kulriya, P.K.; Pivin, J.C.; Chandra, R.; Avasthi, D.K. Blue-Shifted SPR of Au Nanoparticles with Ordering of Carbon by Dense Ionization and Thermal Treatment. *Plasmonics* **2013**, *8*, 295–305. https://doi.org/10.1007/s11468-012-9389-6.
59. Nair, K.; Mitra, S.S. Electrical properties and hopping transport in amorphous silicon carbide films. *J. Non-Cryst. Solids* **1977**, *24*, 1–17. https://doi.org/10.1016/0022-3093(77)90057-6.
60. Anwar, M.S.; Bukhari, S.Z.A.; Ha, J.H.; Lee, J.; Song, I.-H.; Kim, Y.-W. Controlling the electrical resistivity of porous silicon carbide ceramics and their applications: A review. *Int. J. Appl. Ceram. Technol.* **2022**, *19*, 1814–1840. https://doi.org/10.1111/ijac.14034.
61. Choi, W. Optical, structural, and electrical properties of amorphous silicon carbide films. In *Silicon-Based Material and Devices*; Elsevier: Amsterdam, The Netherlands, 2001; pp. 1–71. https://doi.org/10.1016/B978-012513909-0/50003-9.
62. Fujita, S.; Sasaki, A. Dangling Bonds in Memory-Quality Silicon Nitride Films. *J. Electrochem. Soc.* **1985**, *132*, 398–402. https://doi.org/10.1149/1.2113850.
63. Zhou, D.; Huang, L.; Yuan, J.; Li, C. Influences of different sputtering current on the microstructure and electrical properties of silicon nitride thin films deposited on cemented carbide tools. *Ceram. Int.* **2021**, *47*, 32160–32167. https://doi.org/10.1016/j.ceramint.2021.08.108.